

Probing High-Energy Light Dark Matter with IceCube

Gang Guo,^{1,*} Yue-Lin Sming Tsai,^{1,2,†} and Meng-Ru Wu^{1,3,4,‡}

¹*Institute of Physics, Academia Sinica, Taipei, 11529, Taiwan*

²*Key Laboratory of Dark Matter and Space Astronomy,*

Purple Mountain Observatory, Chinese Academy of Sciences, Nanjing 210008, China

³*Institute of Astronomy and Astrophysics, Academia Sinica, Taipei, 10617, Taiwan*

⁴*National Center for Theoretical Sciences, Physics Division, Hsinchu, 30013, Taiwan*

(Dated: April 8, 2020)

The direct detection of particle dark matter through its scattering with nucleons is of fundamental importance to understand the nature of DM. In this work, we propose that the high-energy neutrino detectors like IceCube can be used to uniquely probe the DM–nucleon cross-section for high-energy DM of \sim PeV, up-scattered by the high-energy cosmic rays. We derive for the first time strong constraints on the DM–nucleon cross-section down to $\sim 10^{-32}$ cm² at this energy scale for sub-GeV DM candidates. Such independent probe at energy scale far exceeding other existing direct detection experiments can therefore provide useful insights complementary to other searches.

arXiv:2004.03161v1 [astro-ph.HE] 7 Apr 2020

* gang23@gmail.com

† smingtsai@gate.sinica.edu.tw

‡ mwu@gate.sinica.edu.tw

I. INTRODUCTION

The existence of dark matter (DM) revealed by cosmological and astrophysical observations through its gravitational effect has been firmly established. However, the particle physics nature of DM remains elusive despite tremendous experimental efforts over the past decades with both the direct and indirect detection methods. In particular, the ton-scale underground detectors probing the interaction between DM and atomic nucleus set very stringent limit on the DM–nucleon cross-section down to $\sigma_{\chi p} \sim 10^{-46}$ cm² for DM mass between 10 GeV $\lesssim m_\chi \lesssim$ 10 TeV, approaching the limit set by the neutrino background [1–4]. Recently, increasing amount of work also started to investigate other motivated DM candidates whose masses lighter than GeV with very different experimental techniques and/or cosmological/astrophysical observation, see e.g., sub-GeV DM [5–18], QCD axion DM [19–23], sterile neutrino DM [24–30], and ultralight Bosonic DM [31–36].

Among those, Refs. [10–12] pointed out that the collision of the diffuse cosmic rays (CRs) with energy up to a few GeV in our Milky Way (MW), including nuclei and electrons/positrons, with DM in the halo can up-scatter a small amount of DM to velocities far exceeding values carried by the locally virialized DM [10–12]. This up-scattered DM component with higher velocities can produce larger recoils for targets in existing DM or neutrino experiments than the local DM and gives rise to new exclusions to the DM–nucleon(electron) cross-section for keV $\lesssim m_\chi \lesssim$ GeV, inaccessible by DM experiments without considering this component.

In this paper, we consider the acceleration of light DM by high-energy (HE) CRs with energy of \sim few PeV. The HECRs in this energy range can accelerate DM to very high energy of $E_\chi \lesssim$ PeV. These ultra-relativistic DM can then masquerade as HE neutrinos when they scatter inelastically with nucleons¹ in HE neutrino detectors, such as the IceCube Neutrino Observatory [37] or KM3NeT [38]. In particular, the deep-inelastic scattering (DIS) of DM in ice or water will predominantly produce cascade events, but not the tracks associated with muons. As astrophysical neutrinos traversing cosmological distances are expected to have nearly equal flux in each flavor: $F_{(\nu_e + \bar{\nu}_e)} : F_{(\nu_\mu + \bar{\nu}_\mu)} : F_{(\nu_\tau + \bar{\nu}_\tau)} \simeq 1 : 1 : 1$ [39], one naturally expects that the extra contribution from HE DM masquerading as HE neutrinos can produce an excess in cascade events at some specific energy ranges and angular directions while deviate the flavor ratio from equi-partitioned. Consequently, unique constraints on DM–nucleon cross-section at energy range of $E_\chi \sim$ TeV–PeV in the rest frame of nucleon can be obtained, which will be useful when combined with constraints derived at other energy scales [10–12].

Below in Sec. II, we first compute the up-scattered DM flux in this energy range by the HECRs inside our galaxy as well as the DM flux accelerated by the extragalactic HECRs as a diffuse source. In Sec. III, we derive new constraints on DM–nucleon cross-section at energy range of TeV–PeV using the released HE neutrino data from the IceCube. We discuss the implication and conclude the paper in Sec. IV.

II. ULTRA-RELATIVISTIC DM UPSCATTERED BY HECRS

A. Galactic HE DM flux

Following Refs. [10–12], we assume the galactic HECRs are uniformly and isotropically distributed in a thick disk with a radius of $R = 10$ kpc and a half-height $h = 1$ kpc. We use the observed local CR spectrum shown in Fig. 29.8 of Ref. [40], which follows a broken power over a wide energy range up to 10^{21} eV². For simplicity, we only consider contributions from protons and scale the CR flux above ~ 100 TeV in [40] by a factor of 0.3 to match the well-measured local CR proton flux below ~ 100 TeV [41]. We neglect the small velocity of DM and simply assume them at rest initially.

The differential DM flux (in unit of GeV⁻¹ cm⁻² s⁻¹ sr⁻¹) up-scattered by CRs and arriving at Earth is given by a line-of-sight (l.o.s.) integral [10–12]

$$\Phi_\chi^{\text{MW}}(E_\chi, \Omega) \equiv \frac{d^2 N_\chi}{dE_\chi d\Omega}(E_\chi, \Omega) = \int_{\text{l.o.s.}} dl \int dE_p \frac{\rho_\chi(r)}{m_\chi} \Phi_p(E_p) D_{p\chi}(E_p, E_\chi) \sigma_{p\chi}, \quad (1)$$

where $\Phi_p \equiv dN_p/dE_p$ is the differential flux of CRs (in unit of GeV⁻¹ cm⁻² s⁻¹ sr⁻¹) and ρ_χ is the halo DM mass density. For ρ_χ , we take the Navarro-Frenk-White (NFW) profile [42, 43] with a scale radius $r_s = 20$ kpc, normalized to the local DM density $\rho_0 = 0.3$ GeV cm⁻³ where the Sun is located at $r = 8.5$ kpc from the galactic center (GC). We

¹ We assume the same cross-section for DM–proton and DM–neutron scattering.

² Note that there are different measurements in Fig. 29.8 of Ref. [40], which could differ from each other by a factor of 2. We use the Grigorov and CASA-MIA data below PeV and the mean values of all the measurements above.

note that the single-component DM scenario is assumed in this work so that the DM local density is entirely made of χ . The transfer function $D_{p\chi}(E_p, E_\chi)$ encodes the produced spectrum of up-scattered DM with total energy E_χ from scattering with a CR proton of energy E_p . Assuming that the scattering is elastic and isotropic in the center-of-mass (c.m.) frame,

$$D_{p\chi}(E_p, E_\chi) = \frac{\Theta[E_\chi^{\max}(E_p) - E_\chi]}{E_\chi^{\max}(E_p)}, \quad (2)$$

with

$$E_\chi^{\max} \simeq \frac{E_p}{1 + (m_p^2 + m_\chi^2)/(2m_\chi E_p)}, \quad (3)$$

for $E_p \gg m_p, m_\chi$ in the energy range of concern in this work.

Note that the scattering c.m. energy \sqrt{s} could be as large as 10 GeV for $m_\chi \gtrsim 100$ keV. In this case, inelastic scattering can occur to allow multiple-meson production. We argue, however, that the transfer function in Eq. (2) should still provide a good estimation of the up-scattered E_χ . The reason is that the inelastic scatterings are dominated by resonant channels at low energies and DIS at high energies, and both can be effectively described by a $2 \rightarrow 2$ scattering process (see, e.g., Refs. [44, 45] for nucleon excited by photon and neutrino). Without otherwise stated, we stick to the expression in Eq. (2) throughout this work.

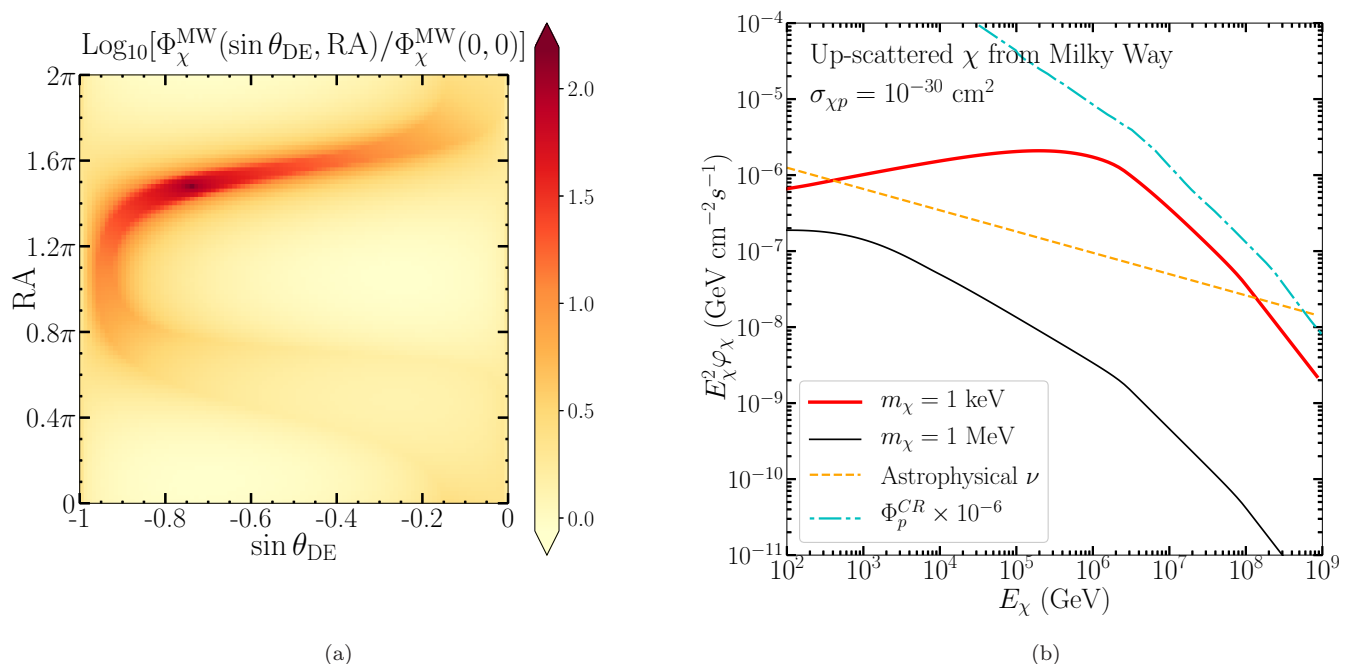


FIG. 1. (a) The angular distribution of DM flux $\Phi_\chi^{\text{MW}}(E_\chi, \Omega)$ up-scattered by CR protons in the Milky Way as a function of the spherical equatorial coordinates $\sin \theta_{\text{DE}}$ and RA , normalized by the value at $\sin \theta_{\text{DE}} = 0$ and $\text{RA} = 0$. (b) The up-scattered DM energy spectrum $E_\chi^2 \varphi_\chi(E_\chi) \equiv E_\chi^2 \int d\Omega \Phi_\chi^{\text{MW}}(E_\chi, \Omega)$ assuming a DM–proton scattering cross-section $\sigma_{\chi p} = 10^{-30} \text{ cm}^2$. The thick-red-solid and thin-black-solid lines are for $m_\chi = 1 \text{ keV}$ and $m_\chi = 1 \text{ MeV}$, respectively. Also shown are the CR proton flux (cyan dash-dotted line) and the best-fit HE astrophysical neutrino flux measured by IceCube (orange dashed line).

The l.o.s. integral in Eq. (1) can be easily computed in the galactic coordinate system. To compare with the IceCube data, we re-express the differential DM flux in the spherical equatorial coordinate, and use right ascension (RA) and declination (θ_{DE}) to describe the arriving angles of DM. In Fig. 1, we show the resulting angular distribution of up-scattered DM flux in panel (a), as well as their energy spectra (integrated over Ω) in panel (b) for cases with $\sigma_{\chi p} = 10^{-30} \text{ cm}^2$ and $m_\chi = 1 \text{ keV}$ (red line) and 1 MeV (black line). The angular distribution shown in panel (a) is normalized by the flux at $\text{RA} = \sin \theta_{\text{DE}} = 0$ and shows clearly that most of the up-scattered DM come from directions within the red-ish band which spans over the disk wherein CRs are confined. In particular, the angular distribution

peaks at the direction of the GC with RA = 1.48π and $\sin\theta_{\text{DE}} = -0.48$. Note that this distribution is independent of the chosen m_χ and $\sigma_{\chi p}$ because they can be factored out.

The energy spectra, however, show strong dependence on m_χ . Using Eqs. (1)–(3), it is straightforward to show that the DM energy spectrum $\int d\Omega\Phi_\chi^{\text{MW}} \propto E_\chi^{-(\gamma_p+1)/2}$ for $E_\chi \ll (m_p^2 + m_\chi^2)/(2m_\chi)$, where γ_p is the CR spectral index characterizing the CR spectra $\Phi_p \propto E_p^{-\gamma_p}$ around $E_p \sim E_\chi$. On the other hand, for $E_\chi \gg (m_p^2 + m_\chi^2)/(2m_\chi)$, $\int d\Omega\Phi_\chi^{\text{MW}} \propto E_\chi^{-\gamma_p}$. The break at $E_\chi \sim (m_p^2 + m_\chi^2)/(2m_\chi)$ originates from the maximum DM energy E_χ^{max} that can be accelerated by CR with energy E_p shown in Eq. (3). This behavior is best illustrated by the red curve in Fig. 1(b) which breaks at $E_\chi \sim 0.5$ PeV for $m_\chi = 1$ keV (see the rescaled Φ_p shown in the same panel for comparison). Comparing the two curves with $m_\chi = 1$ keV and 1 MeV, Fig. 1(b) also shows that for a larger m_χ , the resulting DM flux is smaller as the halo DM number density is inversely proportional to m_χ . On the other hand, the difference between them becomes smaller at $E_\chi \lesssim 0.5$ GeV due to the break of spectrum for $m_\chi = 1$ keV.

B. Extragalactic HE DM flux

The up-scattered DM of extragalactic origin can come from different sources. First, the accelerated DM produced within all other galaxies by the CRs trapped therein by the same mechanism discussed in Sec. II A can arrive the Earth as a diffuse source. Second, the extragalactic HE CRs propagating in the intergalactic space can also up-scatter the cosmic DM without undergoing the gravitational collapse to form galaxies. Both components will arrive as isotropic and diffuse HE DM sources and are indistinguishable. We argue, however, that the first extragalactic component is always subdominant compared to the galactic flux. For example, if we assume all galaxies produce HE DM particles at a same rate, \dot{N}_χ , as the Milky Way, and neglect all the effects due to cosmic evolution and expansion. The energy-integrated flux arriving at the Earth from other galaxies is

$$\begin{aligned} \int dE_\chi \Phi_\chi &\sim \int_0^{r_{\text{max}}} \frac{\dot{N}_\chi n_{\text{galaxy}}}{4\pi r^2} 4\pi r^2 dr \\ &\sim 0.1 \frac{\dot{N}_\chi}{(10 \text{ kpc})^2} \left[\frac{n_{\text{galaxy}}}{0.1 (\text{Mpc})^{-3}} \right] \left[\frac{r_{\text{max}}}{10 \text{ Gpc}} \right]. \end{aligned} \quad (4)$$

Taking $n_{\text{galaxy}} \sim 0.1 \text{ Mpc}^{-3}$ which is the typical number density for small galaxies between 10^7 and $10^{10} M_\odot$ [46], Eq. (4) indicates that the HE DM flux from this component should be at least a factor of 10 smaller than the galactic flux $\sim \dot{N}_\chi / (\text{a few kpc})^2$. Although the higher star forming activities for galaxies at high red-shift may enhance this flux by a factor of a few (see below), it can be compensated by the cosmic expansion as well as the lower DM density inside smaller galaxies. Thus, we only focus on the HE DM produced in the intergalactic space hereafter, which, we show later, can have a higher flux compared to the galactic component.

Similar to the galactic case, the flux of up-scattered DM (in unit of $\text{GeV}^{-1} \text{ cm}^{-2} \text{ s}^{-1} \text{ sr}^{-1}$) from collision between the diffuse intergalactic HE CRs and the cosmic DM background can be expressed as

$$\Phi_\chi^{\text{EG}}(E_\chi) = \int dE_p \int_0^\infty dz \sigma_{p\chi} n_\chi^0 (1+z)^4 F(E_p, z) D_{p\gamma}(E_p, E_\chi(1+z)) \left| \frac{cdt}{dz} \right|, \quad (5)$$

where $|dt/dz|^{-1} = H_0(1+z)[\Omega_\Lambda + \Omega_M(1+z)^3]^{1/2}$. For the cosmological parameters, we take $H_0 = 70 \text{ km s}^{-1} \text{ Mpc}^{-1}$, $\Omega_\Lambda = 0.7$, and $\Omega_M = 0.3$. The current cosmic DM number density is estimated to be $n_\chi^0 \simeq 10^{-6} (\text{GeV}/m_\chi) \text{ cm}^{-3}$ and the corresponding DM density at redshift z is enhanced by a factor of $(1+z)^3$. Another enhancement factor of $(1+z)$ in Eq. (5) accounts for the compression of the energy scale due to the cosmic expansion.

For the diffuse CR flux $F(E_p, z)$ at redshift z , since the attenuation due to the interaction with the cosmic microwave background (CMB) or the diffuse IR/UV background is negligible for protons with energy below $\sim 10^{18}$ eV [47], it is simply given by

$$F(E_p, z) = \frac{c}{4\pi} \int_z^\infty S(z') \frac{1+z'}{1+z} F_{\text{inj}}\left(\frac{1+z'}{1+z} E_p\right) \left| \frac{dt}{dz'} \right| dz', \quad (6)$$

where $F_{\text{inj}}(E_p)$ is the injected CR spectrum per unit time and per unit co-moving volume (in unit of $\text{GeV}^{-1} \text{ cm}^{-3} \text{ s}^{-1}$), and $S(z)$ accounts for the cosmological evolution of the sources. As the spectrum of the extragalactic HE CRs at our interested energy range $E_p \lesssim 10^{18}$ eV is unknown, below we consider sources of ultra-high-energy CRs (UHECRs), namely, CRs with energies above $\sim 10^{18}$ eV, and extrapolate the injected spectrum down to $E_p \sim \text{PeV}$ following a broken power law. It should also be pointed out that in Eq. (6) we have neglected the time for CRs to escape from

the galaxies that produce them. For CR protons at ~ 10 GeV, the escape time is about 10–100 Myr [48]. Assuming that the escape time decreases as $E_p^{-\delta}$ with $\delta \sim 0.3$ – 0.6 [49], PeV CR protons can diffuse out the galaxies within a few Myr, which is much shorter than the cosmological time scales.

The origin of the UHECRs still remains a mystery. Particularly, depending on the mass composition, there are different scenarios that are able to explain the observed features of UHECRs, including an ankle at energy around 5×10^{18} eV as well a sharp drop of the spectrum at 3×10^{19} eV [50, 51]. Assuming a pure proton composition for the UHECRs, the ankle and the cutoff can be explained naturally by the pair production and photohadronic processes of protons on the CMB (the so-called *dip model*) [47]. An alternative model, the *mixed composition model* [52], interprets the ankle as a transition between two different types of components, a steep spectrum at low energy with a proton-dominated composition and a hard one at high energy with increasing fractions of heavy isotopes. The flux suppression at the highest energies is due to the photo-disintegration of heavy nuclei on the CMB and/or the maximum accelerated energy [52]. Despite this ambiguity in modeling the UHECRs, both models tend to indicate a very similar injected proton-dominated flux around 10^{18} eV relevant to this work. Thus, we only consider the dip model from Refs. [53, 54] in the rest of this section.

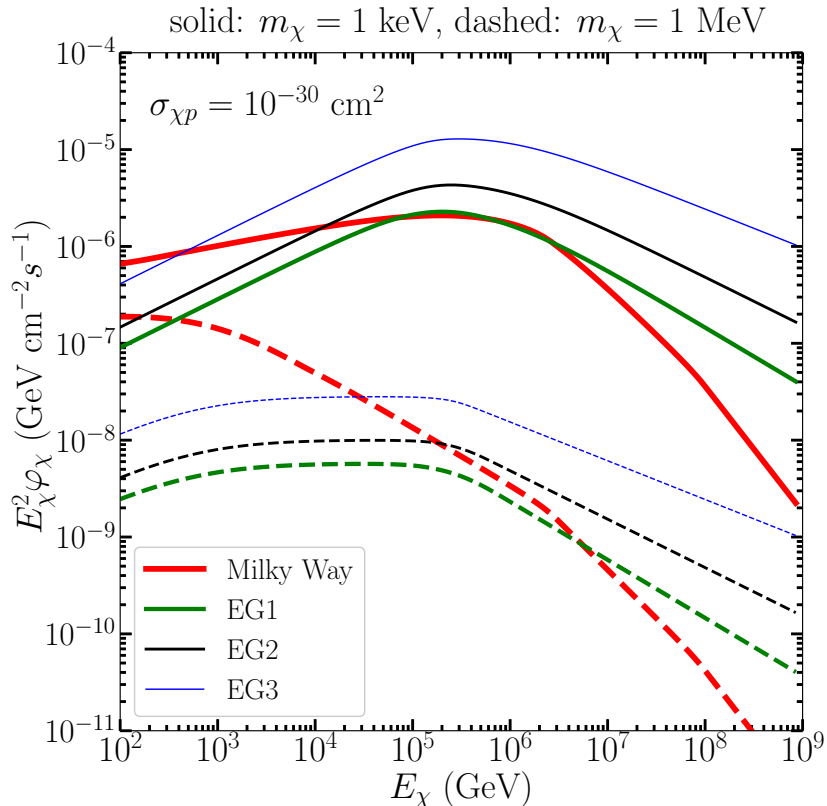


FIG. 2. The DM energy spectrum up-scattered by extragalactic CR protons. The three cases EG1 (green lines), EG2 (black lines), and EG3 (blue lines) assuming different cosmological evolution history of the CR source injection (see text for details) are shown together with the DM spectrum up-scattered by CRs within the Milky Way (red lines). The solid and dashed lines are for $m_\chi = 1$ keV and $m_\chi = 1$ MeV, respectively. The DM–proton scattering cross-section is fixed to 10^{-30} cm².

We assume that the injected protons follow a broken power law, a hard spectrum at low energies followed by a soft one at high energies:

$$F_{\text{inj}}(E_p) = \frac{dN_{\text{inj}}}{dE_p} = N_0 \begin{cases} E_c^{-\gamma+2} E_p^{-2}, & E_p < E_c, \\ E_p^{-\gamma}, & E_p \geq E_c. \end{cases} \quad (7)$$

The normalization constant N_0 and the spectral index γ are tuned to fit the observed UHECRs taking into account the CR propagation in the intergalactic medium. The breaking energy E_c is a free parameter mainly constrained by CR observation. However, a E_c that is as low as a few GeV would require an energy budget beyond known astrophysical

sources [47] Throughout this work, we simply take $E_c = 10^{15}$ eV. For the dip model, we consider the following three cases with different spectral indexes and cosmological evolution history, which all fit the UHECR data well [54].

- Model EG1: $\gamma = 2.6$ and there is no source evolution, i.e., $S(z) = 1$.
- Model EG2: $\gamma = 2.5$ and $S(z)$ follows the star formation rate (SFR),

$$S(z) = \begin{cases} (1+z)^{3.4}, & z \leq 1, \\ 2^{3.7} \times (1+z)^{-0.3}, & 1 < z \leq 4, \\ 2^{3.7} \times 5^{3.2} \times (1+z)^{-3.5}, & z > 4. \end{cases} \quad (8)$$

- Model EG3: $\gamma = 2.4$ and a stronger cosmological evolution of the sources,

$$S(z) = \begin{cases} (1+z)^5, & z \leq 1.7, \\ 2.7^5, & 1.7 < z \leq 2.7, \\ 2.7^5 \times 10^{2.7-z}, & z > 2.7. \end{cases} \quad (9)$$

The corresponding source emissivities at redshift $z = 0$,

$$\mathcal{L}_0 = \int_{10^{16} \text{ eV}}^{10^{23} \text{ eV}} dE_p F_{\text{inj}}(E_p), \quad (10)$$

required to reproduce the observed data are $\mathcal{L}_0 \simeq 1.5 \times 10^{46}$, 6×10^{45} , and 3×10^{45} erg Mpc $^{-3}$ yr $^{-1}$ for the three different models, respectively. From the values of \mathcal{L}_0 , the normalization constant N_0 for F_{inj} can be determined [see Eq. (7)].

Fig. 2 shows the HE DM energy spectra predicted by the three models for $\sigma_{\chi p} = 10^{-30}$ cm 2 and $m_\chi = 1$ keV and 1 MeV. Similar to the galactic case, the extragalactic DM flux also shows a spectral break at $E_\chi \sim (m_p^2 + m_\chi^2)/(2m_\chi)$. For all three models, the extragalactic HE DM flux can be comparable or a factor of a few higher than the galactic component. Model EG3 predicts a largest flux, followed by the model EG2 and EG1, due to the larger contribution at redshift $z \simeq 1-2$.

III. ANALYSIS AND RESULTS

The HE DM particles up-scattered by collision with galactic and extragalactic CRs discussed in the previous Section can generate cascade events in IceCube, which are indistinguishable from the ones induced by neutrinos. We use the IceCube 6-year high energy starting events (HESE), i.e., those with interaction vertex contained within the detector, to constrain the up-scattered DM signals [55–58]. There are in total 80 events with deposited energy above ~ 20 TeV 3 , among which, 53 are cascades and 27 are tracks. If produced by neutrinos, the cascades are due to the neutral current (NC) interaction of all flavors as well as the charged current interactions of $\nu_{e,\tau}$, $\bar{\nu}_{e,\tau}$. On the other hand, the tracks are associated with μ^\pm produced from $\nu_{\mu,\tau}$ and $\bar{\nu}_{\mu,\tau}$ CC interactions.

Since the HE DM scattering with targets can mimic the cascade events, one can obtain a conservative limit on $\sigma_{\chi p}$ by requiring the total cascade events caused by DM not exceeding the observed IceCube data, as done in Refs. [10–12]. In this work, we take a more comprehensive approach by explicitly considering the cascades and tracks from atmospheric muons/neutrinos as well as from astrophysical neutrinos. This leaves less room for the DM signals and thus would result in tighter constraints on $\sigma_{\chi p}$. As the galactic HE DM flux contains a strong angular dependence (see Fig. 1), we also take into account the arrival-angular information of the IceCube events.

In what follows, we will take a binned likelihood analysis to probe/constrain the DM signals. We first discuss how to estimate the event numbers from the atmospheric background, the astrophysical neutrinos, as well as the up-scattered DM. We also discuss specifically how to choose the optimal bins for the deposited energy at IceCube, E_d , the arriving angles, $\sin \theta_{\text{DE}}$ and RA. We then construct the binned likelihood function and obtain the limits on $\sigma_{\chi p}$ using the up-scattered DM from within the Milky Way and from the intergalactic space.

³ Two additional events were found to be coincident with cosmic muons and have been excluded from our analysis.

A. Backgrounds: atmospheric background and astrophysical neutrinos

Backgrounds to astrophysical neutrino searches are dominated by atmospheric muons and neutrinos produced from CR showers, each of which contributes about 25.2 and 15.6 events to the 6 years of IceCube data, respectively [58]. A purely atmospheric explanation for the IceCube data has been already excluded at 8σ [59], indicating the existence of astrophysical neutrinos. However, to probe the up-scattered DM signals with IceCube, the atmospheric muons/neutrinos and astrophysical neutrinos all need to be considered as background sources.

We directly use the estimated background of atmospheric muons/neutrinos from the IceCube paper analysing a 3-year-data set of HESEs [56], where the distributions in arrival angles and deposited energies are available. As for astrophysical neutrinos, we rely on the flux measured by the throughgoing muons (TGM) [60, 61]. Assuming a single power-law for neutrino energy E_ν ranging from a few TeV to 10 PeV, the best-fit flux per flavor for the TGM events is [61]

$$\Phi_{\nu+\bar{\nu}}(E_\nu) = N_{\nu,0} \left(\frac{E_\nu}{100 \text{ TeV}} \right)^{-\gamma_{\nu,0}} \cdot 10^{-18} \text{ GeV}^{-1} \text{ cm}^{-2} \text{ s}^{-1} \text{ sr}^{-1}, \quad (11)$$

where

$$N_{\nu,0} = 1.44_{-0.24}^{+0.25} \quad \text{and} \quad \gamma_{\nu,0} = 2.28_{-0.09}^{+0.08}. \quad (12)$$

Note that the above analysis assumes that fluxes arriving at IceCube are equally partitioned among all neutrino flavors, which naturally arises from the averaged oscillation of neutrinos produced by pion decay from a distant astrophysical source. Detailed studies also showed that the current IceCube data are consistent with the flavor equipartition scenario [39, 62], though a recent study from [63] favours neutron decay as the production mechanism. Unless otherwise stated, we always take the flavor equipartition assumption and use the diffuse per-flavor neutrino flux in Eq. (11) to estimate their contribution to the 6-year HESE data set. If the HE neutrinos detected at IceCube are truly from neutron decay, more cascades will be expected from the astrophysical neutrinos, which only makes our derived constraints in Sec. III C even stronger.

B. Events in each bin from the background and the up-scattered DM

We use the tables of effective areas from Ref. [64] to calculate the event numbers from the astrophysical neutrinos. The effective areas encode the probability of detecting neutrinos with an incoming energy, E_ν , an arriving declination angle, θ_{DE} , and a deposited energy, E_d , at IceCube. They also depend on the neutrino flavor, f , the interaction channel, c , and the event topology, t . In the effective area tables provided by IceCube, E_ν ranges from 10^2 GeV to 10^9 GeV and is divided into 100 bins with equal size in logarithmic scale. Similarly, 20 equal-size bins between $E_d = 10^2$ GeV and 10^8 GeV are taken logarithmically. For θ_{DE} , $\sin \theta_{\text{DE}}$ is divided into 10 equal bins with a bin size of 0.2. Using the effective areas, the expected event numbers of astrophysical neutrinos in given bins of E_ν , deposited energy, E_d , and the declination, $\sin \theta_{\text{DE}}$ can be obtained (see details in Appendix A 1).

To perform a binned likelihood analysis of the observed IceCube events, one can simply take the same bins of E_d and $\sin \theta_{\text{DE}}$ as those in the IceCube effective area tables, which would, however, lead to a very limited statistics. Therefore, we try to combine bins in E_d or $\sin \theta_{\text{DE}}$ to better utilize the data for obtaining the constraint. Moreover, due to the strong angular dependence of the galactic HE DM flux, a further binning in RA in addition to $\sin \theta_{\text{DE}}$ could help enhance the sensitivity. In our analysis, we consider events with $50 \text{ TeV} \leq E_d \leq 100 \text{ PeV}$, $-1 \leq \sin \theta_{\text{DE}} \leq 0$, and $0 \leq \text{RA} \leq 2\pi$. Note that we only include the downgoing events in order to maximize the ratio of DM signals to the astrophysical neutrino signals, since the Earth absorption is typically stronger for DM with the $\sigma_{\chi p}$ range of concern. We use one bin for E_d , and the same bins for $\sin \theta_{\text{DE}}$ as in the effective area tables. For probing the galactic HE DM, we compare two different cases, one without binning in RA and the other with four equal bins. We will show later that using four RA-bins results in a tighter limit due to a strong angular dependence of the galactic HE DM flux. The bin numbers with the corresponding ranges within each bin chosen for E_d , $\sin \theta_{\text{DE}}$, and RA are summarised in Table I. Combining the events computed with the original bins listed in the effective area tables, we can obtain the expected event number from the astrophysical neutrinos in our chosen bins.

To compute the number of HE DM induced cascade events at IceCube, we can first obtain a similar effective area table for DM detection at IceCube as for the HE neutrinos. The attenuation of DM due to χ - p scattering when traversing the Earth needs to be taken into account as for the astrophysical neutrinos. Note that regeneration effect needs to be considered for ν_τ ($\bar{\nu}_\tau$) due to τ^\pm production and decay, but not for the case of $\nu_{e,\mu}$ and DM. For this purpose, we estimate the effective area for HE DM by scaling the effective area for cascade production from the NC

Scenarios	E_d	$\sin \theta_{DE}$	RA
Milky Way	1	5	1
	1	5	4
EG-1,2,3	1	5	1

TABLE I. Number of bins chosen for the binned likelihood analysis in this study. The ranges covered are: $50 \text{ TeV} \leq E_d \leq 100 \text{ PeV}$, $-1 \leq \sin \theta_{DE} \leq 0$, and $0 \leq \text{RA} \leq 2\pi$, respectively. Both the $\sin \theta_{DE}$ and RA are always divided into bins with equal sizes.

interaction of ν_e using the same bins. Similarly, the event numbers of DM in our chosen bins can be obtained. More relevant details are presented in Appendix A 2.

Taking a total exposure time of $T = 2,077$ days and summing over the E_d bins, we show in Fig. 3 the angular distribution of the galactic HE DM induced down-going cascade events ($\sin \theta_{DE} < 0$) for a benchmark case with $m_\chi = 1 \text{ keV}$ and $\sigma_{\chi p} = 10^{-30} \text{ cm}^2$. In contrast to the fairly isotropic distribution of the HE neutrino induced cascades, it shows strong angular dependence on both the RA and DE due to the reason discussed in Sec. II A. As expected, the angular bin containing the most events includes the direction pointing to the GC at $\text{RA} = 1.48\pi$ and $\sin(\theta_{DE}) = -0.48$. Thus, taking into account the angular distribution of the events should lead to a better constraint on $\sigma_{\chi p}$ when considering the galactic DM component, as will be shown in the next section.

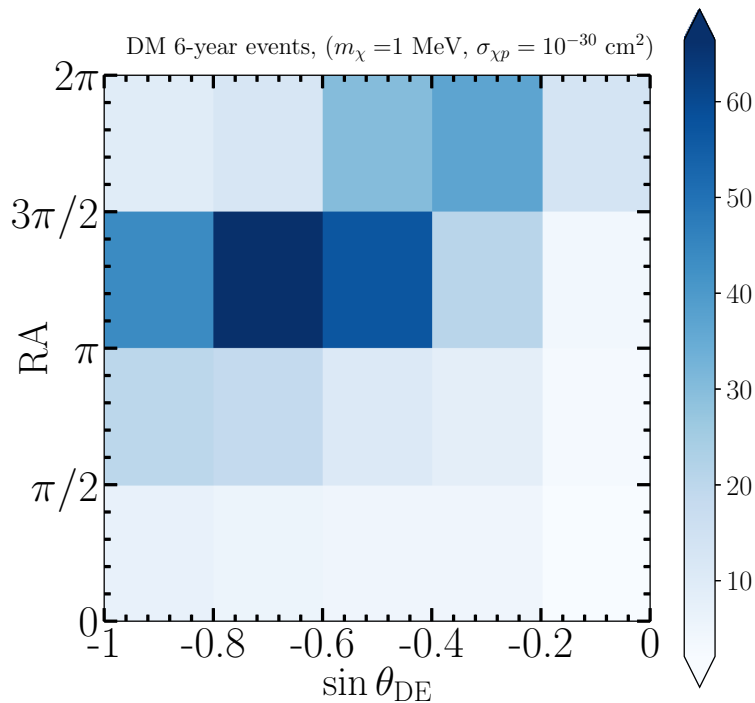


FIG. 3. The two dimensional histogram showing the number of HE DM events that would be detected by IceCube in each bin on the $(\sin \theta_{DE}, \text{RA})$ plane, assuming $m_\chi = 1 \text{ MeV}$ and $\sigma_{\chi p} = 10^{-30} \text{ cm}^2$. Only the up-scattered DM by the galactic CRs are considered for this plot. The bin containing the most events includes the direction towards the galactic center.

C. Constraints on the DM–nucleon scattering cross-section at TeV–PeV

In this section, we perform a binned likelihood analysis by combining the atmospheric muon/neutrino background and the astrophysical HE neutrinos, together with the predicted DM events produced by both the galactic and extragalactic sources, to derive constraints on $\sigma_{\chi p}$. Note that as the c.m. energy of χ – p collision required to accelerate DM to \sim PeV is lower than that related to detecting a PeV DM at IceCube by a factor of m_p/m_χ , the involved $\sigma_{\chi p}$ can generally be different at these two sites due to its energy dependence. Below, we assume that $\sigma_{\chi p}$ is energy-independent following Refs. [10–12] for most cases. We further discuss how the excluded region varies when an energy-dependent cross-section is considered for both the galactic and extragalactic HE DM.

We define the likelihood from our binned data as

$$\mathcal{L}(m_\chi, \sigma_{\chi p}) = \max_{N_\nu, \gamma_\nu} \left[e^{-\frac{1}{2}(\chi_{N_\nu}^2 + \chi_{\gamma_\nu}^2)} \times \prod_{k,m,t} \frac{e^{-(s_{kmt} + b_{kmt})} (s_{kmt} + b_{kmt})^{N_{kmt}}}{N_{kmt}!} \right], \quad (13)$$

where s_{kmt} and b_{kmt} are the expected event numbers from HE DM and the background (including the atmospheric muons/neutrinos and the astrophysical neutrinos), respectively, in the k -th bin of $\sin\theta_{\text{DE}}$ and the m -th bin of RA (see Tab. I)⁴, and N_{kmt} is the corresponding observed event number at IceCube in the same bins. The parameter t stands for the event type, which includes track and cascade. As discussed in Sec. III A, we rely on the flux measured using the TGMs to estimate the event numbers from the astrophysical neutrinos. To account for the flux uncertainty, we introduce the nuisance parameters N_ν and γ_ν , corresponding to the normalization and the spectral parameter of the astrophysical neutrino flux, respectively [see Eq. (12)]. In our likelihood function, we profile out the nuisance parameters with the Gaussian distributions, i.e., $\chi_{N_\nu}^2 \equiv (N_\nu - \bar{N}_\nu)^2 / \sigma_{N_\nu}^2$ and $\chi_{\gamma_\nu}^2 \equiv (\gamma_\nu - \bar{\gamma}_\nu)^2 / \sigma_{\gamma_\nu}^2$, with $\bar{N}_\nu = 1.44$, $\bar{\gamma}_\nu = 2.28$, $\sigma_{N_\nu} = 0.25$, and $\sigma_{\gamma_\nu} = 0.09$ [see Eq. (12)]. Note that both N_ν and γ_ν have asymmetric uncertainties, and we take the larger ones for $\sigma_{N_\nu, \gamma_\nu}$ for conservative studies.

We define the one-sided 95% confidence level (CL) (equivalent to a two-sided 90% CL) for the excluded region by finding where the $-2\Delta \ln(\mathcal{L}) = -2 \ln[\mathcal{L}(m_\chi, \sigma_{\chi p}) / \mathcal{L}(m_\chi, 0)] = 2.71$. Fig. 4 shows the 95% excluded regions on the $(m_\chi, \sigma_{\chi p})$ plane for cases considering the galactic HE DM component. Similar to those derived in Refs. [10–12], for a given m_χ , all the excluded regions have not only lower bounds below which the $\sigma_{\chi p}$ is too small to produce enough HE DM flux and to interact with targets at the IceCube, but also upper bounds above which the Earth absorption effect takes place to prevent enough HE DM reaching the detector. The excluded regions shrink with increasing m_χ and vanish at $m_\chi \gtrsim$ GeV as the DM number density inside the galactic halo decreases with m_χ .

In Fig. 4(a), the solid-red curve and the blue-dashed curve show the excluded regions when taking four and one RA bins (see Tab. I) using the likelihood defined in Eq. (13), respectively. It clearly shows that taking into account the anisotropy of the DM flux helps push the lower bound to smaller values by $\sim 40\%$. In addition, we test the robustness of the excluded region by relaxing the TGM constraint on the astrophysical neutrinos flux for the case with one RA bin and show the resulting blue-dash-dotted curve in the same panel. Specifically, we remove the penalty term, $\exp[-\frac{1}{2}(\chi_{N_\nu}^2 + \chi_{\gamma_\nu}^2)]$, from Eq. (13) and project the excluded region onto the $(m_\chi, \sigma_{\chi p})$ plane by freely varying N_ν and γ_ν . Comparing the blue-dash-dotted curve with the blue-dashed curve, it shows that the derived lower-bound only weakly depends on this assumption by a factor of ~ 2 . We also note that the upper bound at $\sigma_{\chi p} \sim 2 \times 10^{-28} \text{ cm}^{-2}$ for $m_\chi \lesssim 1 \text{ MeV}$ is almost independent of the binning method or the assumption of the astrophysical neutrino flux. This is simply because all the DM are absorbed by the Earth before reaching the IceCube detector located at 1,450 m below the surface when $\sigma_{\chi p}$ is larger than this value. Based on these, we can confidently exclude a wide range of $10^{-32} \text{ cm}^2 \lesssim \sigma_{\chi p} \lesssim 2 \times 10^{-28} \text{ cm}^2$ for $m_\chi \lesssim 10 \text{ keV}$, as well as an extended region for m_χ up to $\sim 1 \text{ GeV}$ when considering the galactic HE DM component only and assuming a constant $\sigma_{\chi p}$ at all relevant energies.

In Fig. 4(b), we show how an energy-dependent $\sigma_{\chi p}$ affects the derived bounds. Taking a simple power-law dependence of $\sigma_{\chi p}$ on E_χ ,

$$\sigma_{\chi p}(E_\chi) = \sigma_{\chi p,0} \times \left(\frac{E_\chi}{100 \text{ TeV}} \right)^\alpha, \quad (14)$$

with $\sigma_{\chi p,0}$ corresponding to $\sigma_{\chi p}$ at $E_\chi = 100 \text{ TeV}$ in the rest-frame of the proton, Fig. 4(b) shows that with a positive (negative) value of $\alpha = 1/3$ ($\alpha = -1/3$), the excluded region shrinks (enlarges) substantially. This is because for light DM considered here, E_χ in the proton-rest-frame at the acceleration site is smaller than that at the IceCube by a factor of $\sim m_p/m_\chi$ as mentioned in the beginning of this subsection. Thus, when we fix $\sigma_{\chi p}$ for different α at $E_\chi = 100 \text{ TeV}$,

⁴ Since we always take one E_d bin, we simply drop out its bin index.

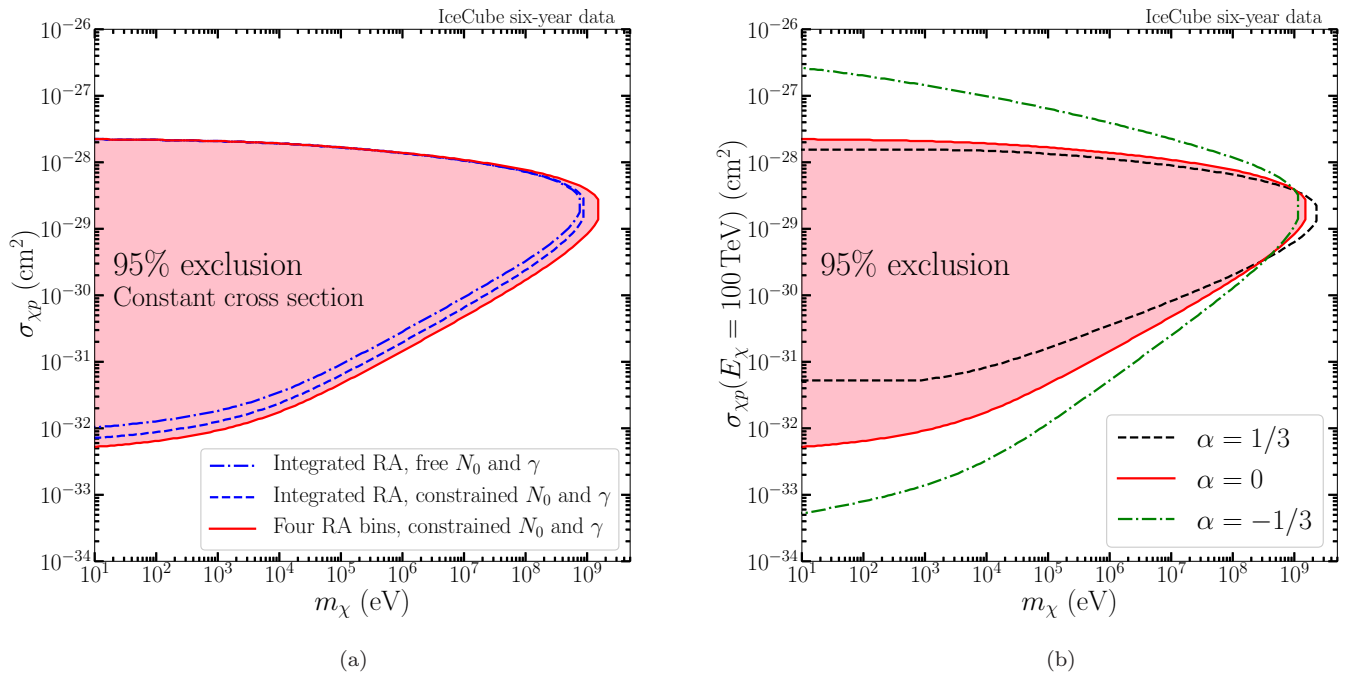


FIG. 4. The 95% exclusion limit projected on the $(m_\chi, \sigma_{\chi p})$ plane considering up-scattered DM by galactic CRs. In panel (a), the excluded regions are derived assuming a constant $\sigma_{\chi p}$ with different numbers of RA bins (see Tab. I) or different assumptions on astrophysical neutrino flux parameters $N_{\nu,0}$ and $\gamma_{\nu,0}$ [see Eq. (12)]. Both the red solid line (four RA bins) and the blue dashed line (one single RA bin) are derived assuming N_0 and γ following Gaussian distributions given by the best fit to the TGM events at the IceCube (see Sec. III A). The blue dash-dotted line (one single RA bin) is obtained without assuming any knowledge for N_0 and γ . In panel (b), we show the derived exclusion limits for $\sigma_{\chi p}$ at $E_\chi = 100$ TeV when an energy-dependent $\sigma_{\chi p} \propto E_\chi^\alpha$ is taken, see Eq. (14). All three lines here are derived taking $N_{\nu,0}$ and $\gamma_{\nu,0}$ distribution given by TGM events.

a positive α results in smaller (larger) values of lower bounds on $\sigma_{\chi p}$ for $m_\chi \lesssim 300$ MeV ($m_\chi \gtrsim 300$ MeV) because the DM flux Φ_χ^{MW} scales proportionally to $\sigma_{\chi p}$ at the acceleration site (see Eq. (1)) and DM with $E_\chi \sim$ PeV contribute the most to the events at IceCube. Likewise, a negative α gives rise to larger (smaller) lower bounds on $\sigma_{\chi p}$ for $m_\chi \gtrsim 300$ MeV ($m_\chi \lesssim 300$ MeV). The same reason also explains why the excluded range in $m_\chi \sim$ GeV around $\sigma_{\chi p} \simeq 10^{-29}$ cm² slightly extends (shrinks) to a larger (smaller) value when α is positive (negative). For the upper bounds, taking $\alpha = 1/3$ results in similar values to the case with $\alpha = 0$ due to the similarly strong absorption at $E_\chi \gtrsim$ PeV. However, for $\alpha = -1/3$, the upper bounds extend to substantially larger value of $\sigma_{\chi p}$ because for $E_\chi \gtrsim$ PeV, it requires larger values of $\sigma_{\chi p}$ at 100 TeV for most DM being absorbed before reaching the IceCube.

We now turn our attention to the HE DM component accelerated by the extragalactic HE CRs (see Sec. II B). Fig. 5 shows the excluded regions derived with three extragalactic models considered in Sec. II B for cases with a constant $\sigma_{\chi p}$ in panel (a) and with energy-dependent $\sigma_{\chi p}$ in panel (b). All three models yield bounds comparable to that derived from the galactic DM component. Note that although the angle-integrated extragalactic DM fluxes from all three models in the relevant energy range exceed that of the galactic component (see Fig. 2), only the model EG3 results in a slightly larger excluded region. This is simply due to the extragalactic HE DM flux being isotropic, unlike the galactic component which has a strong angular dependence. Taking an energy-dependent $\sigma_{\chi p}$ results in similar changes to the excluded regions here as for the case of the galactic DM discussed above.

D. Comparison with existing bounds

The constraints on $\sigma_{\chi p}$ obtained in Sec. III C are very unique because they probe the HE DM interaction with nucleons at $E_\chi \sim$ TeV–PeV. To compare our bounds with those derived from other considerations such as the DM direct detection for nonrelativistic DM or the CR up-scattered DM with $E_\chi \lesssim$ GeV, proper modeling of how $\sigma_{\chi p}$ changes with E_χ is needed. This can depend on the exact nature of interaction of DM with nucleon. Here, we simply

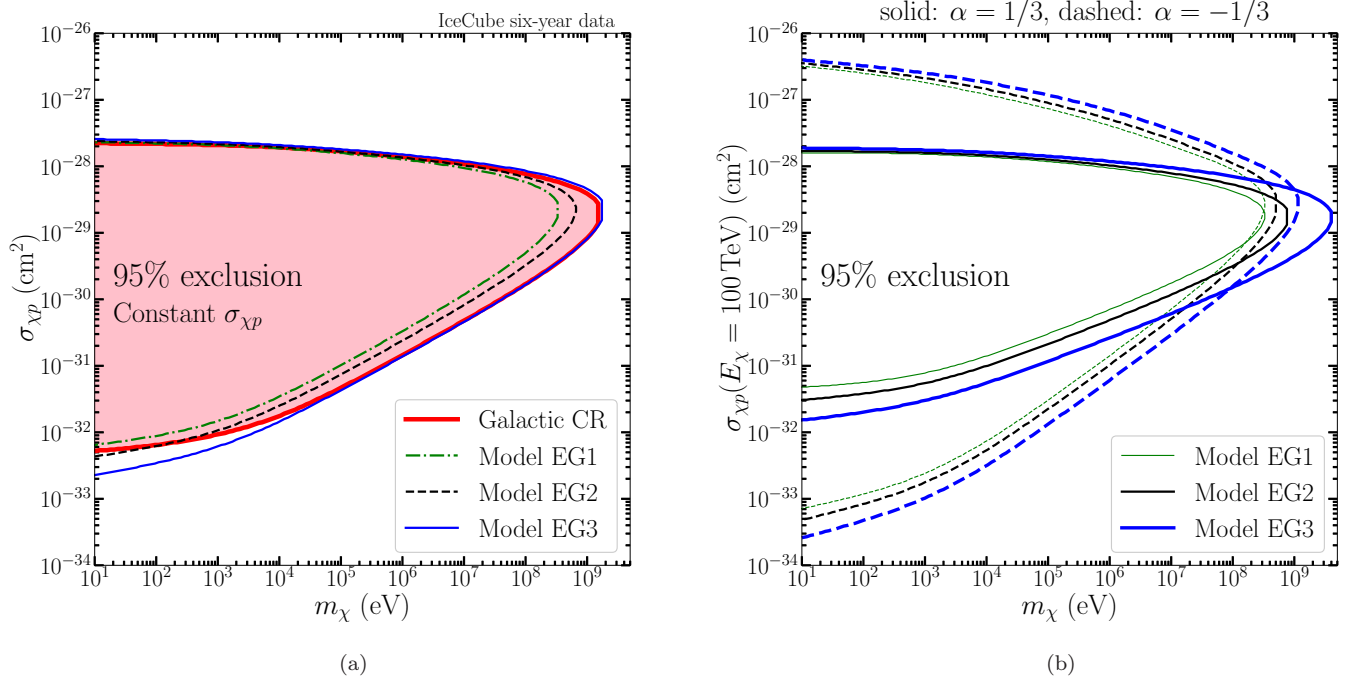


FIG. 5. The 95% exclusion limits projected on the $(m_\chi, \sigma_{\chi p})$ plane derived when considering up-scattered DM by extragalactic CRs. In panel (a), the exclusion contours using different extragalactic CR models EG1, EG2, and EG3 are shown by the green dash-dotted, black dashed, and blue solid line, respectively. Also shown is the red contour obtained by considering the galactic component (see Fig. 4). In panel (b), we show the corresponding exclusion limits assuming an energy-dependent $\sigma_{\chi p}$ as in Fig. 4(b) for $\alpha = 1/3$ and $-1/3$.

take the $\sigma_{\chi p}(E_\chi)$ given in Eq. (14) and extrapolate the excluded regions shown in Fig. 4 to the nonrelativistic regime where the DM velocity $v_\chi = 10^{-3} c$, for cases with constant $\sigma_{\chi p}$ ($\alpha = 0$) and $\alpha = 1/3$. Note that in the nonrelativistic regime, we instead use $\sigma_{\chi p} \propto p_\chi^\alpha$ with p_χ being the momentum of DM.

Fig. 6 shows the results (red and black solid curves) together with different bounds shown in Fig. 7 of Ref. [12]. The bounds labeled by MiniBooNE and XENON1T are given by Ref. [10]. The ones labeled by DayaBay+KamLAND and JUNO are the current and projected limits from Ref. [12]. The grey curve labeled by DD is the limit given by the DM direct detection experiments CRESST [65]. For the constant $\sigma_{\chi p}$ case, the bound that we derived here is comparable to those obtained by considering CR up-scattered DM in energy range of $\sim \text{GeV}$ [10, 12] for $m_\chi \gtrsim 1 \text{ MeV}$ but weaker than the projected sensitivity with JUNO. However, for $m_\chi \lesssim 1 \text{ MeV}$, we improve the existing bounds by roughly one order of magnitude. When we consider energy dependent $\sigma_{\chi p}$ with $\alpha = 1/3$, the excluded region gets shifted to smaller $\sigma_{\chi p}$ by orders of magnitudes (cf. Fig. 4), allowing to exclude $\sigma_{\chi p}$ down to $\sigma_{\chi p} \ll 10^{-32} \text{ cm}^2$ for $m_\chi \lesssim 1 \text{ MeV}$. We note that if the energy dependence of $\sigma_{\chi p}$ resembles the behavior of neutrino–nucleon interaction, we can expect that the excluded region extrapolated to low energy can be pushed to even smaller $\sigma_{\chi p}$.

IV. SUMMARY AND DISCUSSION

In this paper, we have investigated the scenario that light DM particles ($m_\chi \lesssim 1 \text{ GeV}$) can be up-scattered to $\sim 10 \text{ TeV}$ – PeV energy range by the galactic and extragalactic HE CRs and its consequences at the HE neutrino detectors like the IceCube. For a DM–nucleon cross-section $\sigma_{\chi p} \sim 10^{-30} \text{ cm}^2$ at $E_\chi \sim 100 \text{ TeV}$ (in the rest frame of the nucleon), the resulting HE DM fluxes can be comparable to or larger than that of HE neutrinos detected at the IceCube. As these HE DM only produce cascade events in IceCube, differently from HE neutrinos that can also produce tracks, we derive for the first time strong constraints on DM–nucleon cross-section at the energy range of $E_\chi \sim \text{PeV}$ for a wide range of $\sigma_{\chi p}$ and m_χ using the IceCube 6-year HESE sample.

As the DM E_χ at the nucleon rest frame at the acceleration site can differ from that at the detection site by a factor m_p/m_χ , we also explored how an energy-dependent $\sigma_{\chi p}$ affects the derived bounds taking a simple power-law

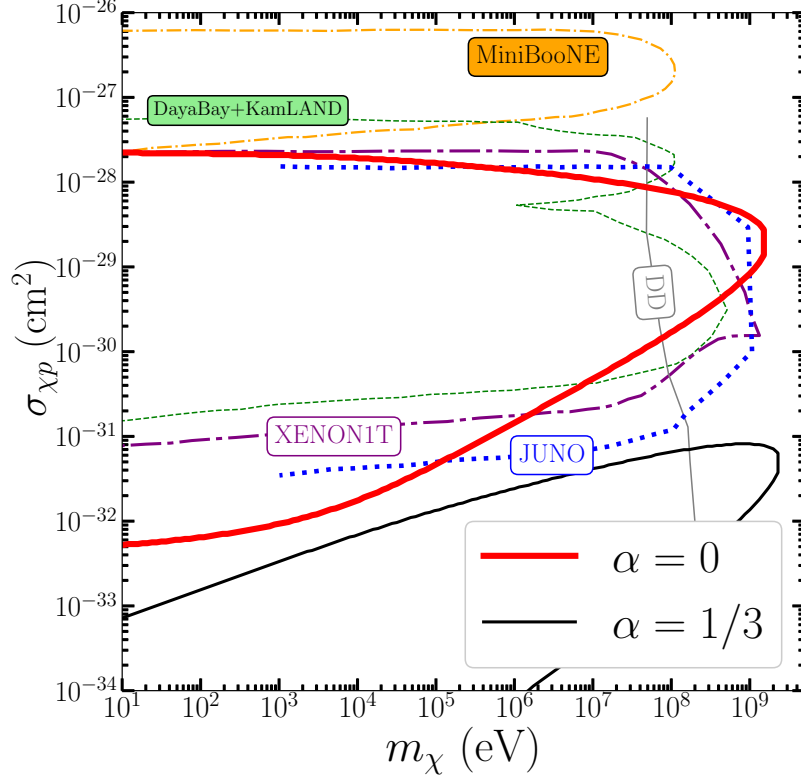


FIG. 6. Comparison of the excluded regions derived in this work with others. Our limits for energy independent ($\alpha = 0$) and energy dependent ($\alpha = 1/3$) cases are shown by red-thick-solid line and black-thin-solid line, respectively. The cross-section of the energy dependent ($\alpha = 1/3$) case has been extrapolated to nonrelativistic regime for DM velocity of $10^{-3}c$, comparable to the local DM velocities. The orange dash-dotted (labeled by MiniBooNE) and purple long dashed lines (labeled by XENON1T) are given by Ref. [10]. The green thin dashed (labeled by DayaBay+KamLAND) and the blue dotted lines (labeled by JUNO) are the current and projected limits from Ref. [12]. The grey curve labeled by DD is the limit given by the DM direct detection experiments CRESST [65].

of $\sigma_{\chi p}(E_\chi)$ beyond the constant $\sigma_{\chi p}$ assumption taken in previous work investigating the up-scattered DM by galactic CRs of \lesssim GeV [10–12]. Taking a positive (negative) power-law index of $1/3$ in the energy dependence of $\sigma_{\chi p}$, we showed that the derived bounds shrink (expand) up to a factor of ~ 10 , depending on m_χ . If naively extrapolating the energy dependence down to low E_χ of the order of MW halo DM, the corresponding constraints on $\sigma_{\chi p}$ can be pushed to even lower values if $\sigma_{\chi p}$ decreases as E_χ . Thus, future work combining existing low-energy limits and our new constraints at high energy with a consistent modeling of the energy dependence of $\sigma_{\chi p}$ can be valuable and will be further pursued.

In this study, we take uniformly distributed galactic CRs and the NFW DM profile. Considering the full spatial dependence of the galactic CR distribution or a different DM halo profile may affect the predicted signal number by a factor of a few. As the signal number depends on $\sigma_{\chi p}^2$, the uncertainties in limits from modeling of the CRs and the DM profile are suppressed by a square root.

We focus on the energy region of TeV–PeV relevant for IceCube. Since the flux of the CRs and HE DM decrease rapidly with a spectral index of ~ -3 , we expect less stringent limits when considering experiments like ANITA [66, 67], which is sensitive to higher energy region around 10^{18} eV. We also note that the up-scatter HE DM signals may possibly alleviate the spectral discrepancy between the IceCube track and cascade datasets [58, 60, 61], although our analysis using the current data only provides a slight improvement. We expect that as increasing amount of data being collected by the IceCube, its future upgrade to IceCube-Gen2, and the upcoming full implementation of KM3NeT, not only further improved constraints can be obtained, hints for light DM signals may also be revealed. Our work here thus highlights that the current and future HE neutrino detectors can probe independently the nature of DM–nucleon interaction at energy scale beyond other experiments.

Throughout this work, we have not considered the inelasticity of DM–nucleon collision, which can produce indirect signals like HE gamma-rays or HE neutrinos from meson-decay. As the flux of such signals only depends on the $\sigma_{\chi p}$ at the collision site of the CRs and DM, the results will not depend on the particular assumption of the energy dependence of $\sigma_{\chi p}$ across a larger energy range and can therefore provide further independent information. Moreover, unlike the constraints derived in this paper which has no sensitivity for large $\sigma_{\chi p}$ due to the absorption of DM by Earth, we expect that $\sigma_{\chi p}$ above certain values will be all excluded by considering these secondary signals. However, production of mesons can depend on the specific DM models. Constraints based on these will be published in a separate work.

ACKNOWLEDGMENTS

We thank Martin Spinrath for providing useful comments to this manuscript. G. G. and M.-R. W. acknowledge support from the Academia Sinica by Grant No. AS-CDA-109-M11. Y.-L. S. Tsai was funded in part by the Chinese Academy of Sciences Taiwan Young Talent Programme under Grant No. 2018TW2JA0005. M.-R. W. acknowledges support from the Ministry of Science and Technology, Taiwan under Grant No. 108-2112-M-001-010, and the Physics Division, National Center of Theoretical Science of Taiwan.

Appendix A: Event numbers from the astrophysical neutrinos and the HE DM

1. Events from the astrophysical neutrinos

The effective area tables for HE neutrinos, $A_{\text{eff},f,c,t}^{ijk}$, are provided by IceCube [64] to calculate the event numbers in bins of the deposited energy, E_d , and arriving angle, θ_{DE} , for a given flux in bins of the incoming neutrino energy, E_ν , with i, j, k being the indices of E_ν -bin, E_d -bin, and $\sin \theta_{\text{DE}}$ -bin, respectively. They also depend on the neutrino flavor, f , interaction channel, c , including the neutral current scattering on nucleon (NC) and charged current scattering on nucleon (CC), as well as the Glashow resonance (GR) for $\bar{\nu}_e$ scattering with electrons, and the event topology, t , which could be cascade or track. It should be pointed out that we have simply assumed a perfect angular resolution for the IceCube detector, i.e., the reconstructed angle is the same as the incoming angle. This assumption only affects our results minorly because the angular bin taken in our analysis has a comparable size as the angular uncertainty, which, for cascades, is about 10° – 15° .

As in the effective area tables, we divide $\sin \theta_{\text{DE}}$ into 10 equal bins with a bin size of 0.2. The energy E_ν in [10^2 GeV, 10^9 GeV] and E_d in [10^2 GeV, 10^8 GeV] are divided into 100 and 20 bins with equal bin size in logarithmic scale. The expected event number of cascades or tracks in each given bin of deposited energy, E_d , and $\sin \theta_{\text{DE}}$ is given by

$$n_{\nu,t}^{jk} = \sum_{i,f,c} [\Phi_{\nu+\bar{\nu}}(E_\nu^i) \Delta E_\nu^i] \times A_{\text{eff},f,c,t}^{ijk} \times \Delta \sin \theta_{\text{DE}} \times 2\pi \times T, \quad (\text{A1})$$

with $\Delta \sin \theta_{\text{DE}} = 0.2$ and $T = 2078$ days during which the IceCube 6-year data were taken.

As discussed in the main text, we bin E_d and $\sin \theta_{\text{DE}}$ differently from that in the effective area tables to obtain better constraints (see also Tab. I). The corresponding event numbers in the new bins can be simply obtained by merging the events given in Eq. (A1). For the cases that RA are divided into four bins, the corresponding event numbers of atmospheric background and astrophysical neutrinos should then be divided by a factor 4, since they are assumed to be uniformly distributed in RA.

2. Events from the up-scattered DM

To compute the number of HE DM induced cascade events at the IceCube, their attenuation due to χ - p scattering when traversing through the Earth needs to be taken into account in the same way as the astrophysical neutrinos. For this purpose, we estimate the effective area for HE DM at the IceCube, $A_{\text{eff},\chi}^{ijkm}$, by scaling the effective area for cascade production from the NC interaction of ν_e in Eq. (A1):

$$A_{\text{eff},\chi}^{ijkm} = A_{\text{eff},\nu_e,\text{NC,cascade}}^{ijk} \frac{\langle e^{-\tau_x} \sigma_{\chi p} \rangle^{ikm}}{\langle e^{-\tau_{\nu_e}} \sigma_{\nu_e p}^{\text{NC}} \rangle^{ikm}}, \quad (\text{A2})$$

where i, j, k are the indices of bins as in Eq. (A1) and we have kept the index of RA-bin, m , for the galactic HE DM flux due to its angular dependence. $\langle e^{-\tau_\alpha} \sigma_{\alpha p} \rangle^{ikm}$ is the averaged value of the product of the survival probability for a given angular and energy bin and the cross-section,

$$\langle e^{-\tau_\alpha} \sigma_{\alpha p} \rangle^{ikm} = \frac{\int_{\sin \theta_{\text{DE}}^{k,\text{min}}}^{\sin \theta_{\text{DE}}^{k,\text{max}}} d \sin \theta_{\text{DE}} \int_{\text{RA}^{m,\text{min}}}^{\text{RA}^{m,\text{max}}} d \text{RA} e^{-\tau_\alpha(E^i, \sin \theta_{\text{DE}})} \sigma_{\alpha p}(E^i) \Phi_\alpha(E^i, \Omega)}{\int_{\sin \theta_{\text{DE}}^{k,\text{min}}}^{\sin \theta_{\text{DE}}^{k,\text{max}}} d \sin \theta_{\text{DE}} \int_{\text{RA}^{m,\text{min}}}^{\text{RA}^{m,\text{max}}} d \text{RA} \Phi_\alpha(E^i, \Omega)}, \quad (\text{A3})$$

with the optical depth given by

$$\tau_\alpha(E, \sin \theta_{\text{DE}}) = N_A \cdot X(\sin \theta_{\text{DE}}) \cdot \sigma_{\alpha p}^{\text{tot}}(E), \quad (\text{A4})$$

for $\alpha = \nu_e$ or χ . In the above equation, N_A is the Avogadro constant, $X(\sin \theta_{\text{DE}}) = \int \rho dl$ is the column depth that DM or neutrino traverses inside the Earth from the declination angle $\sin \theta_{\text{DE}}$, and we take the Earth density from the Preliminary reference Earth model [68]. $\sigma_{\nu_e p}^{\text{tot}} = \sigma_{\nu_e p}^{\text{CC}} + \sigma_{\nu_e p}^{\text{NC}}$ and $\sigma_{\chi p}^{\text{tot}} = \sigma_{\chi p}$ are the total cross-section of ν_e -proton scattering taken from Ref. [69] and the DM-proton cross-section, respectively. Since both the extragalactic HE DM flux and the astrophysical neutrino flux are assumed to be isotropic, the integration over RA in Eq. (A3) is trivial and can be cancelled out. In this case, $\langle e^{-\tau_\alpha} \rangle^{ikm} = \langle e^{-\tau_\alpha} \rangle^{ik}$ and $A_{\text{eff},\chi}^{ijkm} = A_{\text{eff},\chi}^{ijk}$, both independent of the RA-bin index, m . Given the above effective area of the HE DM, we can then compute the corresponding DM induced cascade number at the IceCube in each given bin with the deposited energy E_d^j , $\sin \theta_{\text{DE}}^k$, and $(\text{RA})^m$:

$$n_\chi^{jkm} = \sum_i (\Phi_\chi^{ikm} \Delta E_\chi^i) \times A_{\text{eff},\chi}^{ijkm} \times \Delta \sin \theta_{\text{DE}} \times \Delta \text{RA} \times T. \quad (\text{A5})$$

Similarly to the HE neutrino, the event number of HE DM in the bins chosen for our binned analysis (see Tab. I) can be obtained by combining the events in Eq. (A5).

-
- [1] LUX collaboration, *Results from a search for dark matter in the complete LUX exposure*, *Phys. Rev. Lett.* **118** (2017) 021303 [1608.07648].
- [2] XENON collaboration, *First Dark Matter Search Results from the XENON1T Experiment*, *Phys. Rev. Lett.* **119** (2017) 181301 [1705.06655].
- [3] PANDAX-II collaboration, *Dark Matter Results From 54-Ton-Day Exposure of PandaX-II Experiment*, *Phys. Rev. Lett.* **119** (2017) 181302 [1708.06917].
- [4] XENON collaboration, *Dark Matter Search Results from a One Ton-Year Exposure of XENON1T*, *Phys. Rev. Lett.* **121** (2018) 111302 [1805.12562].
- [5] S. Knapen, T. Lin and K. M. Zurek, *Light Dark Matter in Superfluid Helium: Detection with Multi-excitation Production*, *Phys. Rev.* **D95** (2017) 056019 [1611.06228].
- [6] H. An, M. Pospelov, J. Pradler and A. Ritz, *Directly Detecting MeV-scale Dark Matter via Solar Reflection*, *Phys. Rev. Lett.* **120** (2018) 141801 [1708.03642].
- [7] M. Ibe, W. Nakano, Y. Shoji and K. Suzuki, *Migdal Effect in Dark Matter Direct Detection Experiments*, *JHEP* **03** (2018) 194 [1707.07258].
- [8] M. J. Dolan, F. Kahlhoefer and C. McCabe, *Directly detecting sub-GeV dark matter with electrons from nuclear scattering*, *Phys. Rev. Lett.* **121** (2018) 101801 [1711.09906].
- [9] C. V. Cappiello, K. C. Y. Ng and J. F. Beacom, *Reverse Direct Detection: Cosmic Ray Scattering With Light Dark Matter*, *Phys. Rev.* **D99** (2019) 063004 [1810.07705].
- [10] T. Bringmann and M. Pospelov, *Novel direct detection constraints on light dark matter*, *Phys. Rev. Lett.* **122** (2019) 171801 [1810.10543].
- [11] Y. Ema, F. Sala and R. Sato, *Light Dark Matter at Neutrino Experiments*, *Phys. Rev. Lett.* **122** (2019) 181802 [1811.00520].
- [12] C. Cappiello and J. F. Beacom, *Strong New Limits on Light Dark Matter from Neutrino Experiments*, *Phys. Rev.* **D100** (2019) 103011 [1906.11283].
- [13] A. Berlin, D. Hooper, G. Krnjaic and S. D. McDermott, *Severely Constraining Dark Matter Interpretations of the 21-cm Anomaly*, *Phys. Rev. Lett.* **121** (2018) 011102 [1803.02804].
- [14] LDMX collaboration, *Light Dark Matter eXperiment (LDMX)*, **1808.05219**.
- [15] S. Matsumoto, Y.-L. S. Tsai and P.-Y. Tseng, *Light Fermionic WIMP Dark Matter with Light Scalar Mediator*, *JHEP* **07** (2019) 050 [1811.03292].
- [16] A. Berlin, R. T. D’Agnolo, S. A. R. Ellis, P. Schuster and N. Toro, *Directly Deflecting Particle Dark Matter*, *Phys. Rev. Lett.* **124** (2020) 011801 [1908.06982].

- [17] P. F. Depta, M. Hufnagel, K. Schmidt-Hoberg and S. Wild, *BBN constraints on the annihilation of MeV-scale dark matter*, *JCAP* **1904** (2019) 029 [1901.06944].
- [18] S. A. Hertel, A. Biekert, J. Lin, V. Velan and D. N. McKinsey, *Direct detection of sub-GeV dark matter using a superfluid ^4He target*, *Phys. Rev.* **D100** (2019) 092007 [1810.06283].
- [19] Y. Kahn, B. R. Safdi and J. Thaler, *Broadband and Resonant Approaches to Axion Dark Matter Detection*, *Phys. Rev. Lett.* **117** (2016) 141801 [1602.01086].
- [20] MADMAX WORKING GROUP collaboration, *Dielectric Haloscopes: A New Way to Detect Axion Dark Matter*, *Phys. Rev. Lett.* **118** (2017) 091801 [1611.05865].
- [21] R. T. Co, L. J. Hall and K. Harigaya, *QCD Axion Dark Matter with a Small Decay Constant*, *Phys. Rev. Lett.* **120** (2018) 211602 [1711.10486].
- [22] A. Hook, Y. Kahn, B. R. Safdi and Z. Sun, *Radio Signals from Axion Dark Matter Conversion in Neutron Star Magnetospheres*, *Phys. Rev. Lett.* **121** (2018) 241102 [1804.03145].
- [23] I. Obata, T. Fujita and Y. Michimura, *Optical Ring Cavity Search for Axion Dark Matter*, *Phys. Rev. Lett.* **121** (2018) 161301 [1805.11753].
- [24] E. G. Speckhard, K. C. Y. Ng, J. F. Beacom and R. Laha, *Dark Matter Velocity Spectroscopy*, *Phys. Rev. Lett.* **116** (2016) 031301 [1507.04744].
- [25] M. Drewes et al., *A White Paper on keV Sterile Neutrino Dark Matter*, *JCAP* **1701** (2017) 025 [1602.04816].
- [26] C. A. Argelles, A. Kheirandish and A. C. Vincent, *Imaging Galactic Dark Matter with High-Energy Cosmic Neutrinos*, *Phys. Rev. Lett.* **119** (2017) 201801 [1703.00451].
- [27] V. Brdar, J. Kopp, J. Liu and X.-P. Wang, *X-Ray Lines from Dark Matter Annihilation at the keV Scale*, *Phys. Rev. Lett.* **120** (2018) 061301 [1710.02146].
- [28] A. Caputo, M. Regis and M. Taoso, *Searching for Sterile Neutrino with X-ray Intensity Mapping*, *JCAP* **2003** (2020) 001 [1911.09120].
- [29] F. Hofmann and C. Wegg, *7.1 keV sterile neutrino dark matter constraints from a deep Chandra X-ray observation of the Galactic bulge Limiting Window*, *Astron. Astrophys.* **625** (2019) L7 [1905.00916].
- [30] A. Arza and P. Sikivie, *Production and detection of an axion dark matter echo*, *Phys. Rev. Lett.* **123** (2019) 131804 [1902.00114].
- [31] L. Hui, J. P. Ostriker, S. Tremaine and E. Witten, *Ultralight scalars as cosmological dark matter*, *Phys. Rev.* **D95** (2017) 043541 [1610.08297].
- [32] H. Fukuda, S. Matsumoto and T. T. Yanagida, *Direct Detection of Ultralight Dark Matter via Astronomical Ephemeris*, *Phys. Lett.* **B789** (2019) 220 [1801.02807].
- [33] Y. Chen, J. Shu, X. Xue, Q. Yuan and Y. Zhao, *Probing Axions with Event Horizon Telescope Polarimetric Measurements*, *Phys. Rev. Lett.* **124** (2020) 061102 [1905.02213].
- [34] H.-K. Guo, Y. Ma, J. Shu, X. Xue, Q. Yuan and Y. Zhao, *Detecting dark photon dark matter with Gaia-like astrometry observations*, *JCAP* **1905** (2019) 015 [1902.05962].
- [35] D. Carney, A. Hook, Z. Liu, J. M. Taylor and Y. Zhao, *Ultralight Dark Matter Detection with Mechanical Quantum Sensors*, **1908.04797**.
- [36] H. Davoudiasl and P. B. Denton, *Ultralight Boson Dark Matter and Event Horizon Telescope Observations of M87**, *Phys. Rev. Lett.* **123** (2019) 021102 [1904.09242].
- [37] ICECUBE collaboration, *The IceCube Neutrino Observatory: Instrumentation and Online Systems*, *JINST* **12** (2017) P03012 [1612.05093].
- [38] KM3NET collaboration, *Letter of intent for KM3NeT 2.0*, *J. Phys.* **G43** (2016) 084001 [1601.07459].
- [39] ICECUBE collaboration, *Flavor Ratio of Astrophysical Neutrinos above 35 TeV in IceCube*, *Phys. Rev. Lett.* **114** (2015) 171102 [1502.03376].
- [40] PARTICLE DATA GROUP collaboration, *Review of Particle Physics*, *Phys. Rev.* **D98** (2018) 030001.
- [41] M. J. Boschini et al., *Solution of heliospheric propagation: unveiling the local interstellar spectra of cosmic ray species*, *Astrophys. J.* **840** (2017) 115 [1704.06337].
- [42] J. F. Navarro, C. S. Frenk and S. D. M. White, *The Structure of cold dark matter halos*, *Astrophys. J.* **462** (1996) 563 [astro-ph/9508025].
- [43] J. F. Navarro, C. S. Frenk and S. D. M. White, *A Universal density profile from hierarchical clustering*, *Astrophys. J.* **490** (1997) 493 [astro-ph/9611107].
- [44] A. Mucke, R. Engel, J. P. Rachen, R. J. Protheroe and T. Stanev, *SOPHIA: Monte Carlo simulations of photohadronic processes in astrophysics*, *Comput. Phys. Commun.* **124** (2000) 290 [astro-ph/9903478].
- [45] J. A. Formaggio and G. P. Zeller, *From eV to EeV: Neutrino Cross Sections Across Energy Scales*, *Rev. Mod. Phys.* **84** (2012) 1307 [1305.7513].
- [46] C. J. Conselice, A. Wilkinson, K. Duncan and A. Mortlock, *The Evolution of Galaxy Number Density at $z \lesssim 8$ and Its Implications*, *Astrophys. J.* **830** (2016) 83 [1607.03909].
- [47] V. Berezhinsky, A. Z. Gazizov and S. I. Grigorieva, *On astrophysical solution to ultrahigh-energy cosmic rays*, *Phys. Rev.* **D74** (2006) 043005 [hep-ph/0204357].
- [48] N. E. Yanasak, M. E. Wiedenbeck, R. A. Mewaldt, A. J. Davis, A. C. Cummings, J. S. George et al., *Measurement of the Secondary Radionuclides ^{10}Be , ^{26}Al , ^{36}Cl , ^{54}Mn , and ^{14}C and Implications for the Galactic Cosmic-Ray Age*, *Astrophys. J.* **563** (2001) 768.
- [49] A. W. Strong, I. V. Moskalenko and V. S. Ptuskin, *Cosmic-ray propagation and interactions in the Galaxy*, *Ann. Rev. Nucl. Part. Sci.* **57** (2007) 285 [astro-ph/0701517].

- [50] R. Aloisio, V. Berezhinsky and A. Gazizov, *Transition from galactic to extragalactic cosmic rays*, *Astropart. Phys.* **39-40** (2012) 129 [1211.0494].
- [51] R. Aloisio, *Acceleration and propagation of ultra high energy cosmic rays*, *PTEP* **2017** (2017) 12A102 [1707.08471].
- [52] R. Aloisio, V. Berezhinsky and P. Blasi, *Ultra high energy cosmic rays: implications of Auger data for source spectra and chemical composition*, *JCAP* **1410** (2014) 020 [1312.7459].
- [53] R. Aloisio, D. Boncioli, A. di Matteo, A. F. Grillo, S. Petrerá and F. Salamida, *Cosmogenic neutrinos and ultra-high energy cosmic ray models*, *JCAP* **1510** (2015) 006 [1505.04020].
- [54] R. Alves Batista, D. Boncioli, A. di Matteo and A. van Vliet, *Secondary neutrino and gamma-ray fluxes from SimProp and CRPropa*, *JCAP* **1905** (2019) 006 [1901.01244].
- [55] ICECUBE collaboration, *Evidence for High-Energy Extraterrestrial Neutrinos at the IceCube Detector*, *Science* **342** (2013) 1242856 [1311.5238].
- [56] ICECUBE collaboration, *Observation of High-Energy Astrophysical Neutrinos in Three Years of IceCube Data*, *Phys. Rev. Lett.* **113** (2014) 101101 [1405.5303].
- [57] ICECUBE collaboration, *Observation of Astrophysical Neutrinos in Four Years of IceCube Data*, *PoS ICRC2015* (2016) 1081.
- [58] ICECUBE collaboration, *Observation of Astrophysical Neutrinos in Six Years of IceCube Data*, *PoS ICRC2017* (2018) 981.
- [59] M. Ahlers and F. Halzen, *Opening a New Window onto the Universe with IceCube*, *Prog. Part. Nucl. Phys.* **102** (2018) 73 [1805.11112].
- [60] ICECUBE collaboration, *Observation and Characterization of a Cosmic Muon Neutrino Flux from the Northern Hemisphere using six years of IceCube data*, *Astrophys. J.* **833** (2016) 3 [1607.08006].
- [61] ICECUBE collaboration, *Measurement of the Diffuse Astrophysical Muon-Neutrino Spectrum with Ten Years of IceCube Data*, *PoS ICRC2019* (2020) 1017 [1908.09551].
- [62] S. Palomares-Ruiz, A. C. Vincent and O. Mena, *Spectral analysis of the high-energy IceCube neutrinos*, *Phys. Rev.* **D91** (2015) 103008 [1502.02649].
- [63] A. Palladino, *The flavor composition of astrophysical neutrinos after 8 years of IceCube: an indication of neutron decay scenario?*, *Eur. Phys. J.* **C79** (2019) 500 [1902.08630].
- [64] ICECUBE collaboration, *Atmospheric and astrophysical neutrinos above 1 TeV interacting in IceCube*, *Phys. Rev.* **D91** (2015) 022001 [1410.1749].
- [65] CRESST collaboration, *First results from the CRESST-III low-mass dark matter program*, *Phys. Rev.* **D100** (2019) 102002 [1904.00498].
- [66] ANITA collaboration, *The Antarctic Impulsive Transient Antenna Ultra-high Energy Neutrino Detector Design, Performance, and Sensitivity for 2006-2007 Balloon Flight*, *Astropart. Phys.* **32** (2009) 10 [0812.1920].
- [67] ANITA collaboration, *Constraints on the diffuse high-energy neutrino flux from the third flight of ANITA*, *Phys. Rev.* **D98** (2018) 022001 [1803.02719].
- [68] A. M. Dziewonski and D. L. Anderson, *Preliminary reference earth model*, *Physics of the Earth and Planetary Interiors* **25** (1981) 297 .
- [69] A. Connolly, R. S. Thorne and D. Waters, *Calculation of High Energy Neutrino-Nucleon Cross Sections and Uncertainties Using the MSTW Parton Distribution Functions and Implications for Future Experiments*, *Phys. Rev.* **D83** (2011) 113009 [1102.0691].